ADVANCED MATERIALS
www.advmat.de

Ultrastrong and High Thermal Insulating Porous High-Entropy Ceramics up to 2000 °C

Zihao Wen, Zhongyu Tang, Yiwen Liu, Lei Zhuang, Hulei Yu, and Yanhui Chu**

High mechanical load-carrying capability and thermal insulating performance are crucial to thermal-insulation materials under extreme conditions. However, these features are often difficult to achieve simultaneously in conventional porous ceramics. Here, for the first time, it is reported a multiscale structure design and fast fabrication of 9-cation porous high-entropy diboride ceramics via an ultrafast high-temperature synthesis technique that can lead to exceptional mechanical load-bearing capability and high thermal insulation performance. With the construction of multiscale structures involving ultrafine pores at the microscale, high-quality interfaces between building blocks at the nanoscale, and severe lattice distortion at the atomic scale, the materials with an ≈50% porosity exhibit an ultrahigh compressive strength of up to ≈337 MPa at room temperature and a thermal conductivity as low as ≈0.76 W m^{-1} K^{-1}. More importantly, they demonstrate exceptional thermal stability, with merely ≈2.4% volume shrinkage after 2000 °C annealing. They also show an ultrahigh compressive strength of ≈690 MPa up to 2000 °C, displaying a ductile compressive behavior. The excellent mechanical and thermal insulating properties offer an attractive material for reliable thermal insulation under extreme conditions.

1. Introduction

Porous ceramic materials are of great importance for myriad applications, such as electrodes, photonics, and catalyst supports.[1] They have also attracted growing interest in thermal insulation recently due to their unique physical and chemical properties, such as lightweight, low thermal conductivity, and good chemical inertness.[2–5] Reliable thermal insulation materials under extreme conditions, such as complex mechanical loadings and large thermal gradients in deep-space and deep-earth environments, require an unusual combination of exceptional mechanical load-carrying capability and thermal insulation performance.[6–8] However, these properties are mutually exclusive.[6,9] To be specific, the increase in thermal insulation capacity of porous ceramics (thermal conductivity ≤1 W m^{-1} K^{-1}) can be principally realized by increasing porosity, but it invariably tends to reduce their mechanical strength (often less than 10 MPa or even worse at elevated temperatures).[10] This shortcoming of porous ceramics seriously hinders their applications as thermal insulation materials in extreme environments. Therefore, it is imperative to find ways to simultaneously improve the mechanical strength and thermal insulation capacity of porous ceramics.

The secret to overcoming these trade-offs for porous ceramics lies in the structure design, which can span from microscale to atomic scale.[5,11,12] For various natural high-strength materials such as crustaceans and nacre, they have been discovered to have their smallest building blocks on the submicrometer scale. This is believed to be a biological optimization of mechanical strength, taking advantage of the emerging "size effects."[13,14] Drawing inspiration from this, many man-made porous ceramics have been engineered to comprise submicrometer-sized building blocks, such as submicrofibers measuring just a few hundred nanometers in diameter.[15] Moreover, the thermal insulating performance of porous ceramics can also be improved when their pore sizes are in the submicron range, primarily because of the significant Knudsen effect.[16,17] At the nanoscale, grain interfaces are significant and should be carefully considered.[18] High-quality interfaces, characterized by strong bonding without defects or amorphous phases, can promote the rapid force transfer along the building block and to many other ones through connections upon loading, leading to a significant enhancement of mechanical strength.[15,19] In addition to the microscale and nanoscale design, the newly proposed high-entropy concept at the atomic scale opens up a vast compositional space for fabricating high-strength materials, benefiting from the notable solid-solution strengthening mechanisms induced by lattice distortion.[20–22] Experimentally, a consensus has been reached that the mechanical strength of high-entropy materials outperforms those of their binary components.[23–25] Therefore, by introducing lattice distortion, the mechanical strength of porous ceramics can be enhanced. Additionally, the lattice distortion, combined with high mass disorder originating from the external dopants, can be considered effective thermal insulating barriers, hindering the phonon scattering and lowering thermal conductivity.[26,27] Thus, the key to fabricating high-strength and high thermal insulating

Z. Wen, Z. Tang, Y. Liu, L. Zhuang, H. Yu, Y. Chu
School of Materials Science and Engineering
South China University of Technology
Guangzhou 510641, China
E-mail: lzhuang@scut.edu.cn; chuyh@scut.edu.cn

The ORCID identification number(s) for the author(s) of this article can be found under https://doi.org/10.1002/adma.202311870

DOI: 10.1002/adma.202311870

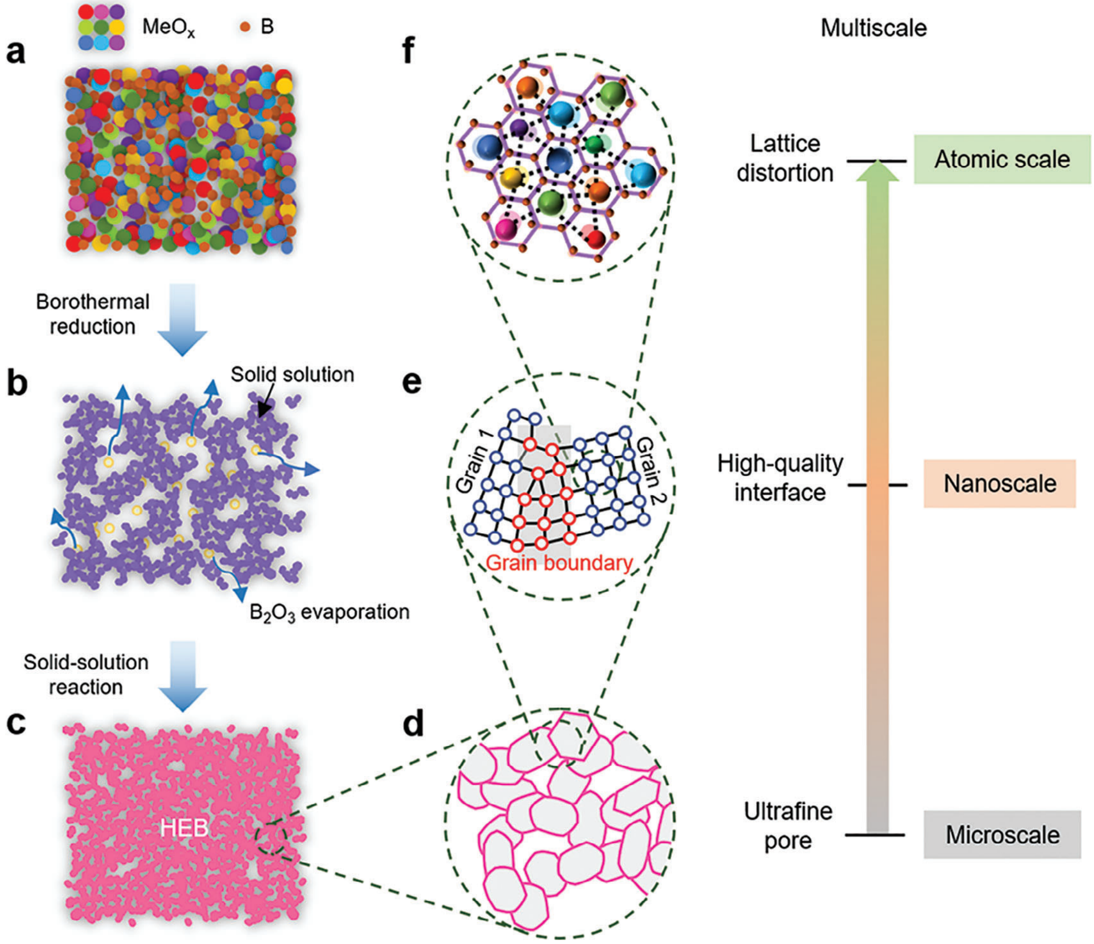

Figure 1. Schematic illustration of the fabrication and the multiscale design of the 9PHEB samples. a) Uniform mixture of the metallic oxides and boron powders with an equimolar ratio. b) Step I: formation of solid solution compounds by borothermal reduction using the UHTS apparatus. c) Step II: formation of single-phase 9PHEB samples using the UHTS apparatus. Multiscale design involving features of d) ultrafine pore, e) high-quality interface, and f) lattice distortion.

porous ceramics lies in a multiscale structure design: i) establishing ultrafine pores at the microscale; ii) forming high-quality interfaces between building blocks at the nanoscale; iii) introducing severe lattice distortion at the atomic scale.

In this work, for the first time, we report a multiscale design and fast fabrication of 9-cation porous high-entropy diboride ($(Hf_{1/9}Zr_{1/9}Ta_{1/9}Nb_{1/9}Ti_{1/9}Cr_{1/9}Mo_{1/9}V_{1/9}W_{1/9})B_2$, 9PHEB) ceramics via a self-made ultrafast high-temperature synthesis (UHTS) apparatus based on strong Joule heat within seconds. Owing to the established microscale ultrafine pores (a majority of 0.8–1.2 µm), high-quality nanoscale interfaces with no defects or amorphous phases, and the severe atomic-scale lattice distortion (mass scattering of 25.33%), our 9PHEB materials with an ≈50% porosity show an ultrahigh compressive strength of up to ≈337 MPa at room temperature and a thermal conductivity as low as ≈0.76 $W\ m^{-1}\ K^{-1}$, which are among the best-reported porous materials. Moreover, the 9PHEB materials also exhibit ultrahigh compressive strength up to 2000 °C with a ductile compressive behavior of a maximum ≈690 MPa strength. All these features demonstrate a reliable material for thermal insulation under extreme conditions.

2. Fabrication

We performed a two-step strategy to fabricate our 9PHEB samples, as illustrated in **Figure 1**. First, the fine boron and transition metallic oxides were uniformly mixed and used as raw materials (Figure 1a). As heated via our self-made UHTS apparatus to a moderate temperature, complex boron compounds were formed within seconds by borothermal reduction. During this process, the substantial generation and escape of B_2O_3 gas resulted in abundant pores left in the compounds. In the second step, the compound products in Figure 1b were ground into powders so that the large pores in the products were destroyed ,while the fine pores were retained. Then, via the UHTS technique, the compounds were sintered at a high temperature, forming strong connections between grains. At the same time, a solid-solution reaction happened in the compounds, leading to the formation of a single HEB phase (Figure 1c). Through these two steps, the multiscale structure design can be realized in the 9PHEB samples. To be specific, the uniform and ultrafine pores at the microscale (Figure 1d), as well as the strong connections and good interfaces between building blocks at the nanoscale (Figure 1e),

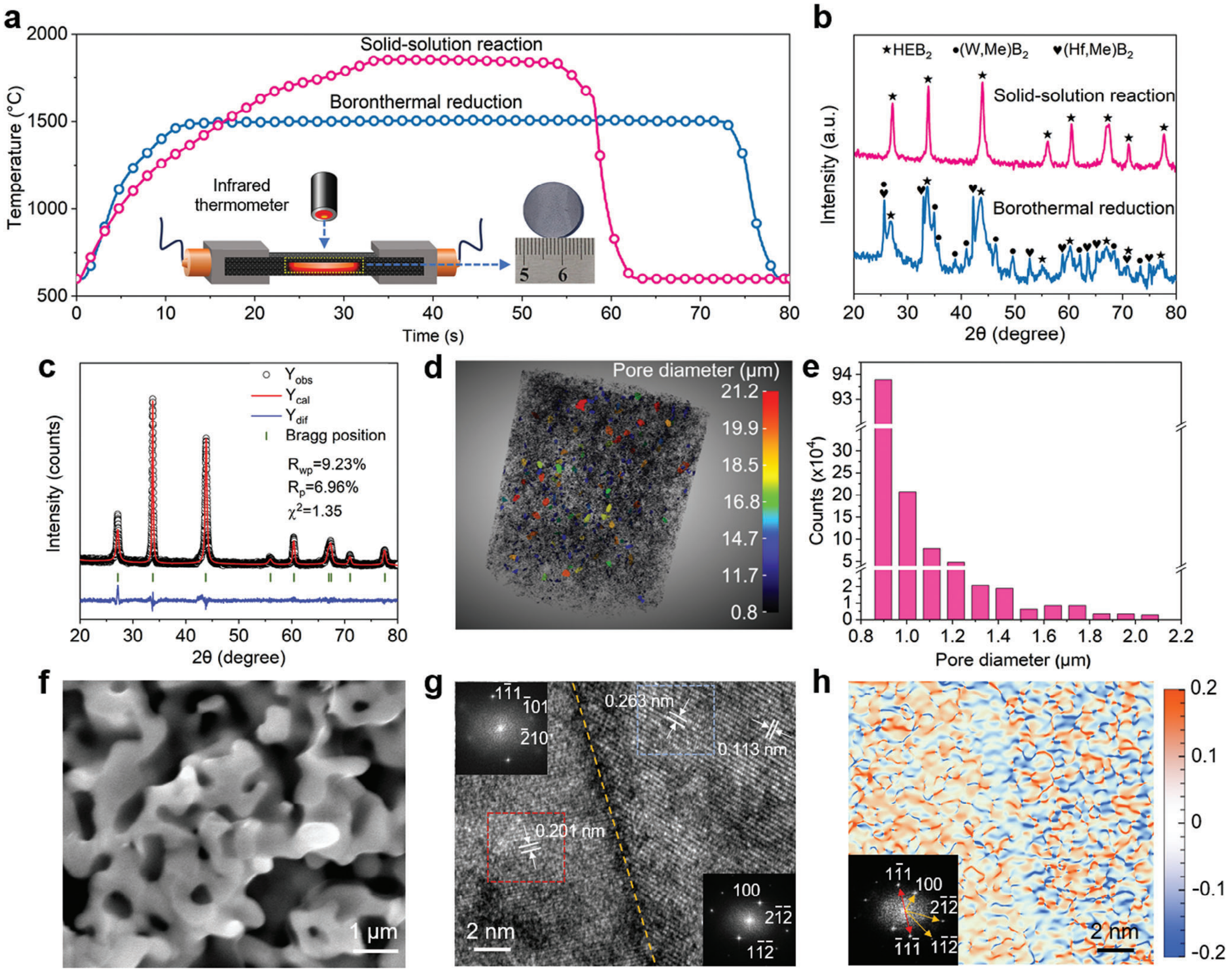

Figure 2. Fabrication and the characterization of the 9PHEB samples. a) Heating temperature versus time profiles via the UHTS apparatus. The insets are the schematic illustration of the apparatus and the photograph of a fabricated sample with ≈50% porosity. b) XRD patterns. c) XRD refinement patterns using GSAS software. d) Reconstructed 3D image of a typical sample from an X-ray microscope. e) Pore size distributions from the reconstructed 3D microstructure. f) SEM image of the samples. g) TEM image of the grains and corresponding FFT maps. h) The atomic elastic strain mapping (normal strain in [100] direction).

can be well established in the 9PHEB samples. Moreover, at the atomic scale, there exists large lattice distortion and mass fluctuation induced by incorporated atoms with different cation radii in the 9PHEB lattices (see Figure 1f). All these features will exert a great influence on the mechanical and thermal performance of the 9PHEB samples.

The porosities of the 9PHEB samples can be tuned by changing the parameters of the UHTS apparatus (the inset of **Figure 2**a). As exhibited in Table S1 (Supporting Information), by increasing the temperatures of borothermal reduction (step I) from 1500 to 1750 °C (Figure S1a, Supporting Information), the total porosities of the 9PHEB samples vary from ≈60% to ≈40%. It is noteworthy that when the borothermal reduction temperatures are too low (such as 1350 °C, Figure S1a, Supporting Information), the fabricated samples are structurally unstable, which indicates that the connections between building blocks are not well established. Regarding the solid-solution reaction (step II, as shown in Figure S1b, Supporting Information), at an inadequate reaction temperature, e.g., 1750 °C, split-phases involving (W, Me)B$_2$, (Hf, Me)B$_2$, and C are presented in the samples from the X-ray diffraction (XRD) pattern (see Figure S2a, Supporting Information). This phenomenon suggests that such a low temperature is insufficient to provide enough driving force and energy for the complete solid-solution reaction. As the temperature increases to 1850 °C (Figure 2a; and Figure S1b, Supporting Information), only HEB peaks can be detected in the XRD patterns, as exhibited in Figure 2b; and Figure S2b (Supporting Information). The corresponding Rietveld refined XRD results were acquired using general structure analysis system (GSAS) software, as shown in Figure 2c. The low fitting factors (R_p = 6.96% and R_{wp} = 9.23%) indicate that the synthesized 9PHEBs have a hexagonal structure with a space group of *P6/mmm*. Besides, the refined unit cell parameters (a = 3.069 Å and c = 3.290 Å) of the 9HEBs are in good accordance with the average values from their individual diborides ($a = 3.056$ Å and $c = 3.302$ Å). These results demonstrate the successful synthesis of the single-phase 9PHEB samples. A typical well-fabricated sample is exhibited in the inset of Figure 2a. Therefore, a conclusion can be drawn that by rationally controlling the borothermal reduction and solid-solution reaction, the single-phase 9PHEB samples with tunable porosities can be acquired.

3. Morphology and Structures

Microstructures of the pores (sizes and distributions) are significant to the properties of porous ceramics. To explore the pore features of the as-synthesized 9PHEB samples, an X-ray microscope was utilized. The reconstructed 3D microstructure is shown in Figure 2d, from which the pore distributions are highly uniform with pore sizes ranging from 0.8 to 21.2 µm. Particularly, among the calculated ≈1 360 000 pores, ≈92% of them fall in 0.8–1.2 µm (Figure 2e). The pore sizes of the 9PHEB samples can be further verified by the mercury intrusion analysis (Figure S3, Supporting Information), which also shows the pores are predominantly submicrometer-sized. These results demonstrate the ultrafine-pore characteristic of the synthesized 9PHEB samples. Figure 2f exhibits the scanning electron microscope (SEM) image of the 9PHEB samples. Clearly, the grains have been well-sintered together, forming seamless and strong connections between them. Figure S4a (Supporting Information) displays the SEM image of the 9PHEB samples after acid etching. Obviously, grain boundaries show up due to the acid etching, exhibiting fine grains with an average size of 1.07 ± 0.31 µm (Figure S4b, Supporting Information). Thus, the applied UHTS technique enables complete sintering between adjacent grains while effectively inhibiting their uncontrolled growth and coarsening, owing to its ultrafast heating rate.[28]

Figure 2g shows a high-resolution transmission electron microscope (HRTEM) image of the as-fabricated 9PHEB samples and the corresponding fast Fourier transform (FFT) maps. It is seen that the grain boundary (see the yellow line) is distinct and clean, with neither amorphous phases nor defects, indicating a well-established interface. In addition, FFT maps (see the insets of Figure 2g) of the grains confirm a typical hexagonal structure. Moreover, the left region of the HRTEM image shows an interplanar spacing of 0.201 nm, corresponding to the representative {111} surface of the hexagonal crystal structure, in accordance with the left FFT results. The right region of the HRTEM image represents two sets of interplanar spacing, namely 0.263 nm corresponding to {100} surface and 0.113 nm corresponding to {212} surface. Furthermore, the crystal cell parameters of these two sets of crystal surface spacing are calculated to be 3.037 and 3.383 Å, respectively, close to the XRD refined results ($a = 3.069$ Å and $c = 3.290$ Å, Figure 2c). These results further confirm the successful fabrication of the 9HEB samples. The atomic elastic strain mapping (normal strain in [100] direction) of the fabricated 9PHEB samples is exhibited in Figure 2h. It is notable that the TEM image in Figure 2g has two grains with different orientations, corresponding to the results pointed out by red and yellow arrows, respectively (see the inset of Figure 2h). Obviously, the lattices suffer from severe distortion due to the incorporated different atoms, which should play a key role in the mechanical and thermal properties of the 9HEB samples. This part will be discussed later. The elemental distributions of the 9PHEB samples were characterized by SEM and TEM equipped with energy dispersive spectroscopy (EDS). Clearly, as shown in **Figure 3a**; and Table S2 (Supporting Information), all nine metal elements are homogeneously distributed at the microscale, with an equimolar ratio. Also, no elemental segregation can be observed at the nanoscale (Figure 3b), suggesting good elemental distributions of our 9PHEB samples.

4. Mechanical Properties

The compressive properties of the fabricated 9PHEB samples at room temperature are displayed in **Figure 4a**. The compressive strengths of the 9PHEB samples are found to increase with the decrease of porosities. To be more specific, at a relatively high total porosity of ≈60% (specifically, 58.2%±3.4%, with a closed porosity of 36.5% ± 9.6%, see Figure S5, Supporting Information), the 9PHEB samples show a relatively low strength of 145±17 MPa (Figure 4a; and Figure S6a–d, Supporting Information). Typically, it is worth noting that at the beginning of the near linear-elastic region, the stress–strain curve is jagged; similarly, after reaching the maximum, the strength drops by steps, following a pseudoductile failure mode. This phenomenon indicates that the connected necks are mechanically weak so that they can progressively bend, buckle, and eventually collapse. However, this neck feature also gives rise to low load-bearing capability. For the 9PHEB samples with a total porosity of ≈50% (specifically, 50.9% ± 2.6%, with a closed porosity of 35.1% ± 5.0%, Figure S5, Supporting Information), with the increase of strain, the mechanical strength steeply rises to 337 ± 43 MPa before dropping dramatically (Figure 4a; and Figure S6b–d, Supporting Information). The compression process of the 9PHEB samples involves the initiation of microcracks, followed by their propagation and eventual penetration throughout the entire samples, as clearly visualized in Figure S7 (Supporting Information). Considering that the 9PHEB samples are made up of building blocks (the open-cell foam model[29]), the bending deflection δ and the structure length L follow a relationship of $\delta \propto \frac{FL^3}{E_s I}$, where F is the force at the middle point of the building block, E_s is the solid modulus of the struct, and I is the second moment of the cross-section area of the building block. For a given F, E_s, and I, the increase of the volume of solid building blocks and the connected necks results in a decrease of L and a drastic decrease in δ of a building block, which reduces the bending capability of the building blocks but increases their rigidity.

As can also be confirmed by in situ SEM observations (see the insets of Figure 4a), the sample tends to fail by "vertical slabbing": a microcrack appears and then grows to form a contiguous vertical failure plane. To reflect the engineering reliability of our 9PHEBs for reliable components, the Weibull distribution regarding the mechanical strength was determined. Eleven samples at a porosity range of 45–55% were tested, and their compressive strengths were recorded and fitted according to Weibull statistics. The fitting results are shown in Figure 4b. It is obvious that all the tested points fall within the 95% confidence band, with a fitting factor (R^2) of 0.98, demonstrating a concentrated distribution of compression strengths. Besides, the Weibull modulus m is measured to be 7.9, indicating that our materials are

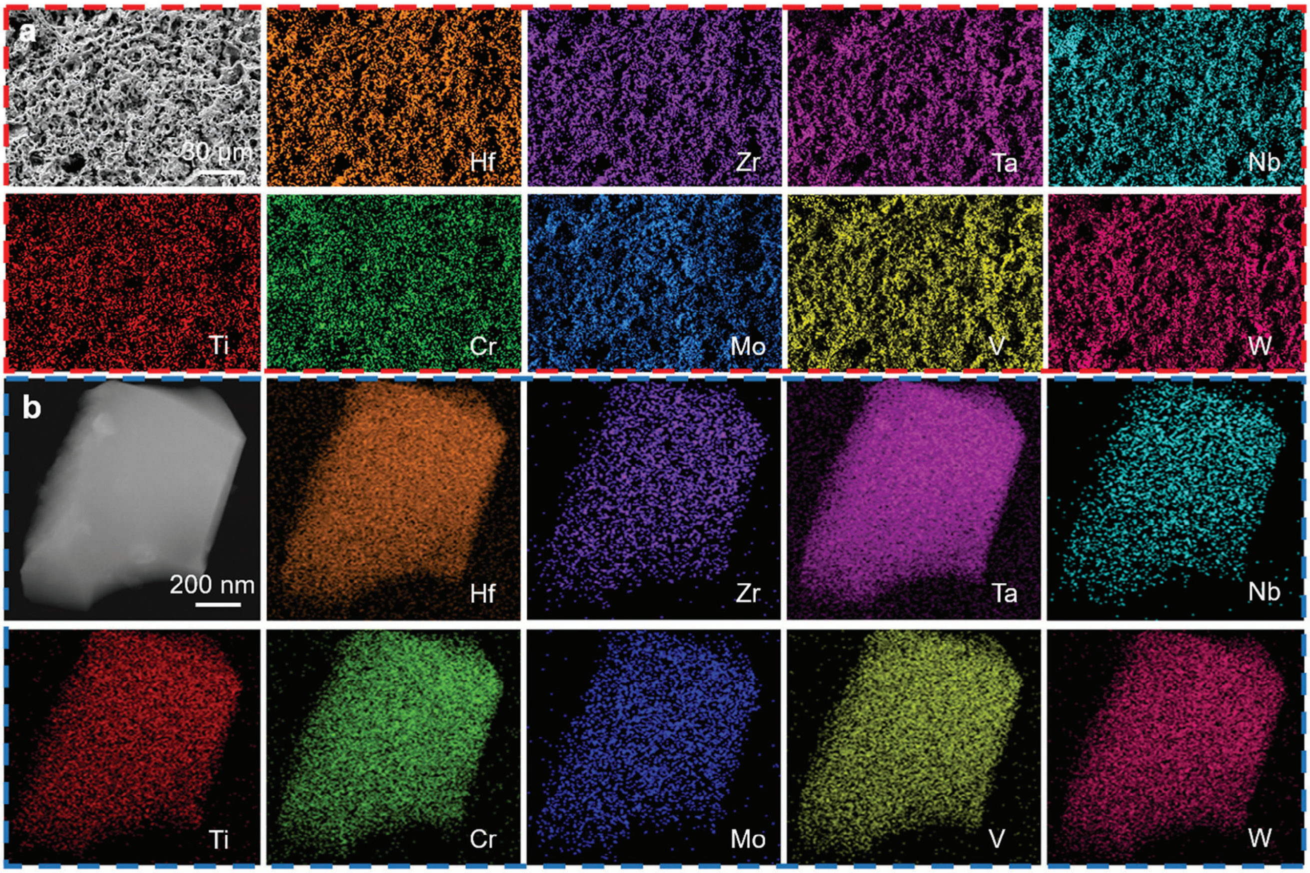

Figure 3. Elemental distributions of the fabricated 9PHEB samples at the micro- and nanoscale. a) SEM image and corresponding EDS mappings. b) The TEM image and corresponding EDS mappings of a grain.

mechanically reliable. When the total porosity of 9PHEB samples is further tailored to ≈40% (specifically, 40.3% ± 2.2%, with a closed porosity of 29.0% ± 8.1%, Figure S5, Supporting Information), the mechanical strength increases up to 507 ± 35 MPa (Figure 4a; and Figure S6c,d, Supporting Information). As can be found in Figure 4c; and Table S3 (Supporting Information), the 9PHEB materials possess significantly higher mechanical strength compared to the reported porous ceramics,[3,15,8,30–53] demonstrating an exceptional load-bearing capability. Therefore, the ultrahigh compressive strength achieved in our 9PHEB samples should benefit from the following reasons: First, as proved in Figure 2d–f, the samples are characterized by ultrafine pores at the microscale, which are firmly connected by abundant well-sintered necks (with high-quality and strong interface between grains at the nanoscale). Thus, upon loading, the force can transfer fast along the building block and to many other ones through the well-connected necks, attributing to homogenous stress distribution and avoiding overload in a certain region. Second, at the atomic scale, the building blocks of our materials are made of solid solutions incorporated with nine elements. The severe lattice distortion (Figure 2h) can largely improve the stiffness and strength of the building blocks, which are also beneficial to the overall load-bearing capability of the 9PHEB samples.[60] Considering the great potential of high-temperature applications of our 9PHEB materials, we proceeded to assess their in situ mechanical behaviors at elevated temperatures. As exhibited in Figure 4d, the stress–strain curve of the 9PHEB samples at 1500 °C displays no significant difference from that at room temperature. The ultimate stress was tested to be 332 MPa (98.5% of the room-temperature strength), suggesting high strength retention of the fabricated 9PHEB samples. When the testing temperature rises to 1800 °C, deviation from linear-elastic-failure behavior can be observed: the stress increases rapidly in the onset (stage I), followed by a slowdown of stress increasing rate (stage II), and then an accelerated increase in stress (stage III). The changes in failure mode should be related to the collapse of architectures and the subsequent resintering of the samples. Specifically, at an elevated temperature, slip motion, and grain-boundary sliding can take place in a crystalline sample.[61] Thus, under loading, the samples can undergo ductile densification (stage II) and eventually be resintered when the ceramic particles are in close contact with one another (stage III). It is worth mentioning that the lattice distortion can act as a barrier to restrict the slip motion of dislocations at elevated temperatures. Hence, the 9PHEB samples with severe lattice distortion exhibit a high strength at 1800 °C (132 MPa at 10% strain and 789 Mpa at 54% strain). With the increase of temperature to 2000 °C (Figure 4d), the strength of the samples is slightly reduced (102 MPa at 10% strain and 692 MPa at 49% strain); additionally, the stress–strain curve becomes smoother (the zigzag has disappeared), demonstrating

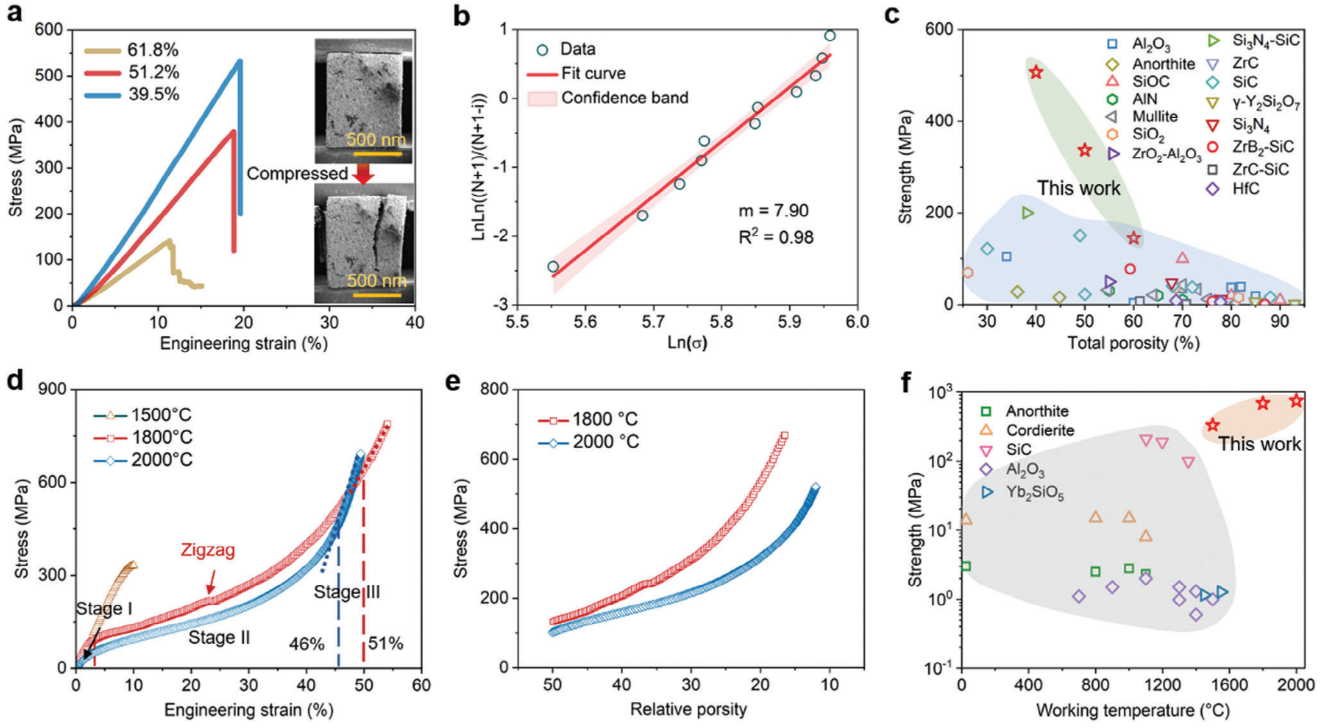

Figure 4. Mechanical properties of the fabricated 9PHEB samples. a) Compressive stress–strain curves of the samples with different porosities. b) Weibull distribution regarding the compressive strength of tested samples at a porosity range of 45–55%. c) Strength versus porosity of the 9HEB samples compared to the reported porous ceramics, such as SiC,[3,15,30–33] mullite,[34–38] Si_3N_4-SiC,[39] Si_3N_4,[40] Al_2O_3,[41] SiO_2,[42,43] ZrB_2-SiC,[44,45] γ-$Y_2Si_2O_7$,[46,47] ZrC,[48,50] ZrC-SiC,[49] HfC,[50] AlN,[51] SiOC,[52] Anorthite,[53] and ZrO_2-Al_2O_3.[8] d) In situ compressive stress–strain curves of the samples at elevated temperatures. e) Stress-relative porosity curves of the samples were tested at 1800 and 2000 °C. f) Strength versus testing temperature of the 9HEBs compared to anorthite,[54] cordierite,[55] Al_2O_3,[56,57] SiC,[58] and Yb_2SiO_5.[59]

the weaker bonding at an elevated temperature.[61] Figure S8 (Supporting Information) exhibits the morphology of the 9HEB samples after testing at 2000 °C. Obviously, their morphology is much denser compared to the initial ones, which indicates the samples have resintered during the high-temperature tests. The ultimate porosities of the samples in situ tested at 1800 and 2000 °C were measured to be 9.1% and 15.0%, respectively. By assuming that the samples have reached their ultimate porosity at the beginning of stage III (namely, the slopes of stress–strain curves are constant), the relationship between stress and relative porosity can be calculated and acquired. As shown in Figure 4e, upon compression at high temperatures, the stress of the samples increases with the decrease in their porosity. In particular, the increase rate (slope) of the samples compressed at 1800 °C is larger than that at 2000 °C, which is in accordance with the weakening effects of atomic bonds at high temperatures. Compared to the reported high-temperature porous ceramics, our synthesized 9PHEBs present a much better compressive strength at elevated temperatures (Figure 4f; and Table S4, Supporting Information),[54–59] demonstrating that they are reliable for use in harsh environments.

5. Thermal Insulation and High-Temperature Stability

Thermal conductivity is another essential factor for thermal insulating materials. Taking the 9PHEB samples with a porosity of ≈50% as an exemplary case study, they possess a low thermal conductivity σ_T of 0.76 W m^{-1} K^{-1} at room temperature (see **Figure 5a**). With the increase of testing temperature to 300 °C, the σ_T value slightly rises to 1.01 W m^{-1} K^{-1}. This is caused by increased thermal radiation heat transfer at elevated temperatures. The specific heat capacity C_p shows a similar trend with σ_T: its value increases from 0.22 to 0.45 J g^{-1} K^{-1}, while the thermal diffusivity α decreases from 0.93 to 0.60 mm^2 s^{-1} as the temperature rises from 25 to 300 °C. Combined with the superior mechanical properties and thermally stability, our 9PHEB materials are comparable to the best porous ceramics reported so far (Figure 5b; and Table S5, Supporting Information),[30,32,37,45,49,50,62–68] exhibiting great potential in thermal insulating applications.

Thermal transport in solid porous materials follows four major modes of heat transfer, i.e., radiation, gas convection, gas conduction, and solid conduction.[69,70] Specifically, thermal radiation refers to the heat transfer through the transmission of electromagnetic waves from objects and surfaces that possess temperatures. However, in practical scenarios where temperatures are below 500 °C, the contribution of radiation is typically negligible.[6] Regarding the gas convection in porous materials, it becomes possible only when the Grashof (*Gr*) number is larger than 1000, according to the following expression

$$Gr = \frac{g\,\alpha\,\Delta T\,d^3 \rho_g}{\eta^3} \tag{1}$$

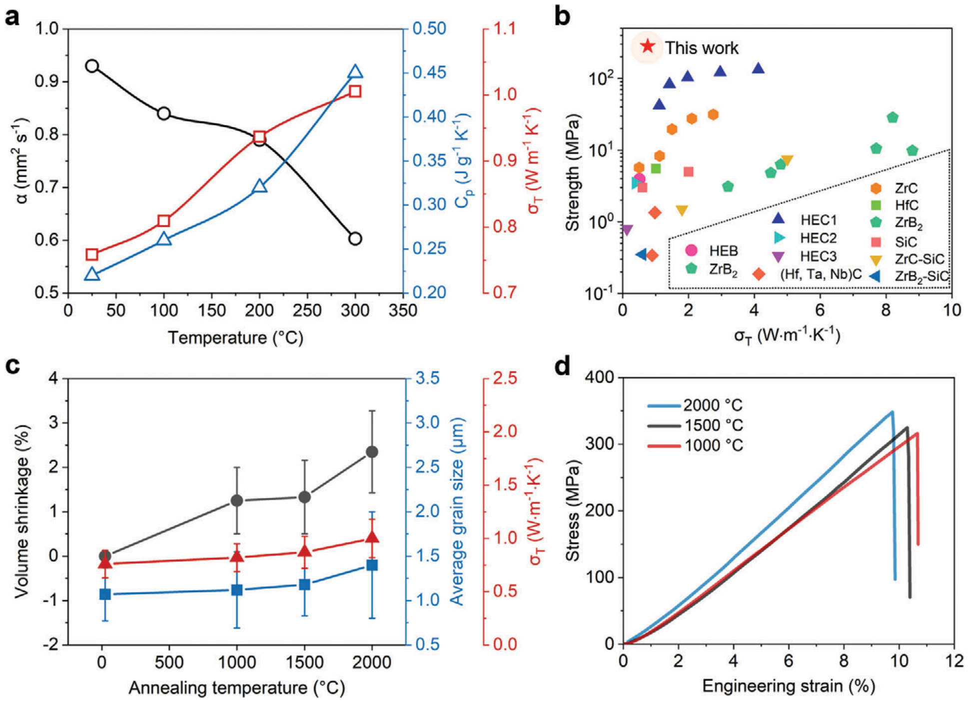

Figure 5. Thermal properties of the fabricated 9PHEB samples. a) Thermal conductivity σ_T, specific heat capacity C_p, and thermal diffusivity α from room temperature to 300 °C. b) Thermal conductivity versus compressive strength compared to other porous ceramic systems, such as SiC,[30,32] Mullite,[37] ZrB$_2$-SiC,[45] ZrC-SiC,[49] HfC,[50] HEB ((Zr$_{0.2}$Hf$_{0.2}$Ti$_{0.2}$Nb$_{0.2}$Ta$_{0.2}$)B$_2$),[62] ZrB$_2$,[63] ZrC,[64] HEC1 ((Ta$_{0.2}$Nb$_{0.2}$Ti$_{0.2}$Zr$_{0.2}$Hf$_{0.2}$)C),[65] HEC2 ((Zr$_{0.2}$Hf$_{0.2}$Ti$_{0.2}$Nb$_{0.2}$Ta$_{0.2}$)C),[66] HEC3 ((Ti$_{0.167}$Cr$_{0.167}$V$_{0.167}$Mo$_{0.167}$Nb$_{0.167}$Ta$_{0.167}$)C),[67] and (Hf, Ta, Nb)C.[68] c) The changes in volume shrinkage, average grain size, and thermal conductivity σ_T of the samples after annealing at 1000, 1500, and 2000 °C. d) Compressive stress versus strain curves of the samples after annealing at 1000, 1500, and 2000 °C.

where g is the gravitational acceleration constant (9.8 m s^{-2}), α is the volume expansion coefficient of the gas, ΔT is the temperature difference across individual pores, d is the pore diameter, ρ_g is the density, and η is the dynamic viscosity of the gas. Apparently, the convection of air at a pressure of 1 atmosphere (Gr ≥1000) requires a pore diameter larger than 10 mm, which is significantly higher than the pore sizes of our 9PHEB samples (Figure 2e). Therefore, the gas convection in our materials is almost completely suppressed. For the gas conduction, it is primarily influenced by the collisions between gas molecules within the internal pores of materials, as well as the interactions between gas molecules and pore walls. Commonly, the gas thermal conduction in thermal-insulation porous materials can be predicted by the Knudsen equation[69]

$$\lambda_g = \frac{\lambda_{g,0} \cdot \Pi}{1 + 2\beta \cdot K_n} \tag{2}$$

where $\lambda_{g,0}$ is the thermal conductivity of free air, Π is the porosity, β is the parameter characterizing the energy transfer that occurs when a gas molecule collides with a solid molecule, and K_n is the Knudsen number, the ratio of the mean free path of gas molecules to the pore size of a material. It is obvious that reducing pore sizes in thermal-insulation materials can depress the heat conduction of gas by restricting the movements and collisions of gas molecules. This phenomenon is known as the Knudsen effect. Previous study has shown that the Knudsen effect significantly emerged when the pore sizes of materials were less than 1 μm.[16] Since our materials possess a comparable average pore size (0.8–1.2 μm), the gas conduction in the 9PHEBs is believed to become much smaller than conventional porous ceramics (with pore sizes of tens to hundreds of micrometers).

With respect to the solid heat conduction, its value is strongly correlated to the skeleton materials. For our 9PHEB skeleton, the incorporated transition metal atoms (nine elements introduction from IVB, VB, and VIB groups) can randomly occupy the cationic sublattice sites, thus inducing large lattice distortion and disorder at the atomic scale. Meanwhile, the differences in atom sizes and binding energy give rise to strong fluctuations of the mass and strain fields (as confirmed in Figure 2h), promoting the phonon scattering and decreasing the thermal conductivity, as proved by the following equation

$$\tau^{-1} = \frac{\delta^3 \omega_D^4}{4\pi v_m^3}\Gamma = \frac{\delta^3 \omega_D^4}{4\pi v_m^3}\left(\Gamma_m + \Gamma_s\right) \tag{3}$$

where τ^{-1} is the thermal barrier factor induced by phonon scattering, δ^3 is the atomic volume, ω_D is the Debye frequency, ν_m is the mean phonon velocity, Γ is the phonon scattering parameter, Γ_m is the phonon scattering parameter caused by mass fluctuations, and Γ_s is the phonon scattering parameter caused by stress fluctuations. It can be clearly seen that the phonon scattering parameter Γ is mainly influenced by Γ_m and Γ_s. In particular

$$\Gamma_m = \sum_i x_i \left(\frac{m_i - \overline{m}}{\overline{m}}\right)^2 \tag{4}$$

where x_i is the percentage of ith element atoms, m_i is the mass of the dopants, and $\bar{m}$ is the average mass of all dopants. For our 9PHEBs, the Γ_m is calculated to be 25.33%, larger than that of the reported 5-cation HEBs with a value of 19.85%.[62] Regarding the fluctuation of the stress field Γ_s, it can also be reflected by the lattice distortion $\bar{\mu}$, based on the following equation

$$\bar{\mu} = \frac{2\sqrt{\sum_i^n \left(a_i^{\text{eff}} - \bar{a}\right)^2} + \sqrt{\sum_i^n \left(c_i^{\text{eff}} - \bar{c}\right)^2}}{3} \qquad (5)$$

where a_i^{eff} and c_i^{eff} are the effective interatomic distances of the ith element, $\bar{a}$ and $\bar{c}$ are the average interatomic distances of n elements, and n is the number of constituent metal elements. Furthermore, the $\bar{\mu}$ of our 9PHEBs is evaluated to be 0.12, larger than that of 5-cation HEBs (0.07).[62] These results suggest that our 9PHEB materials have severe mass fluctuations and lattice distortion with intense phonon scattering and reduced average free path of phonons, which are beneficial to achieving an overall low thermal conductivity.

To explore the feasibility of our 9PHEBs to serve under extreme environments, their thermal stability was investigated up to 2000 °C. As illustrated in Figure 5c; and Figure S9 (Supporting Information), when exposed to temperatures of 1000, 1500, and 2000 °C for 60 min, the volume shrinkages of the samples are very small (merely 1.25% ± 0.75%, 1.33% ± 0.83%, and 2.35% ± 0.92%, respectively). Meanwhile, their grain sizes are measured to be 1.12 ± 0.43, 1.18 ± 0.35, and 1.40 ± 0.60 µm after annealing at 1000, 1500, and 2000 °C, respectively, exhibiting limited grain coarsening compared to the original ones of 1.07 ± 0.31 µm (see Figure 5c; and Figure S10 (Supporting Information), which provide the representation of the samples annealed at 2000 °C). These results suggest the remarkable thermal stability of our synthesized 9PHEBs, which can be attributed to their strong sluggish diffusion effect.[19] Furthermore, the thermal and mechanical properties of the 9PHEB samples after high-temperature annealing were also investigated. Figure 5c illustrates the changes in thermal conductivity σ_T with increasing annealing temperatures. It can be observed that the thermal conductivity values gradually increase from 0.76 ± 0.13 to 1.0 ± 0.18 W m^{-1} K^{-1} when the annealing temperatures increase from room temperature to 2000 °C. This slight increase in thermal conductivity can be explained by the inevitable grain coarsening that occurs during high-temperature treatments, as exhibited in Figure 5c. Regarding the compression properties, the strengths of the 9PHEB samples treated at 1000, 1500, and 2000 °C are 328 ± 35, 308 ± 42, and 356 ± 38 MPa, respectively (see Figure 5d; and Figure S11, Supporting Information). The improvement of strength values for 2000 °C samples might be owing to their minor shrinkage of volume. These results confirm the exceptional high-temperature thermal stability of our 9PHEB samples.

6. Conclusion

In summary, we have successfully fabricated high-performance porous ceramics 9PHEBs with superior mechanical and thermal properties via a simple and effective UHTS technique. The combination of a high mechanical strength (≈337 MPa) at a porosity of ≈50% and a low thermal conductivity (≈0.76 W m^{-1} K^{-1}) endows our 9PHEB materials with great potential as reliable thermal insulation. The superior mechanical and thermal properties are believed to result from the multiscale design: i) the ultrafine pores at the microscale, as well as strong connections and good interfaces between building blocks at the nanoscale, can be well constructed, owing to the ultrafast heating rate and ultrahigh temperature of the UHTS technique; ii) the severe fluctuations of the mass and strain fields induced by the large lattice distortion at the atomic scale, which simultaneously improves the stiffness of lattice and decreases the thermal conductivity of the ceramics by acting as phonon scattering barriers. Moreover, the synthesized 9PHEB show exceptional dimension and strength retention up to 2000 °C, making them suitable for use in extreme conditions.

7. Experimental Section

Fabrication of the 9PHEB Samples: A two-step strategy was applied to fabricate the 9PHEB samples. The transition metal oxide powders, involving HfO_2, ZrO_2, Nb_2O_5, Ta_2O_5, TiO_2, Cr_2O_3, MoO_3, V_2O_5, WO_3, and amorphous boron powders, were used as raw materials. The detailed information of the raw powder materials were listed in Table S6 (Supporting Information). First, these transition metal oxides were equimolarly weighed and then well mixed with 30%-excess boron powders according to the ratio of the reaction equation. Afterward, the mixed powders were pressed into a green body of 16 mm in diameter and 3 mm in height with a pressure of 10 MPa and a holding time of 4 min. The green body was then placed between two pellets of graphite heater (100 × 18 × 4.75 mm^3, AvCarb Felt G475, Fuel Cell Store, USA) of the self-made UHTS apparatus. Subsequently, an alternating current (AC, 100–250 A) was applied to both ends of the pellets to heat the samples to the desired temperatures within seconds under the protection of Ar gas at atmospheric pressure. During this process, borothermal reduction occurred. The as-obtained compounds were then ground into powders to destroy the large pores. Afterward, the powders were remolded and heated via the UHTS apparatus again to form a solid solution. The temperatures of samples heated by the UHTS apparatus were measured by an infrared radiation thermometer (SensorTherm GmbH M313, Germany). More details about the synthesis conditions can be found in Table S1 (Supporting Information). The heating rates of the samples are 80–140 °C s^{-1} (corresponding to 1350–1750 °C) for borothermal reduction, and 30–40 °C s^{-1} (corresponding to 1750–1950 °C) for solid-solution reaction. The temperature-control accuracy was within ±10%.

Materials Characterization: The porosities (including the total and closed ones) of the fabricated 9PHEB samples were measured by Archimedes drainage method. At least five samples were tested at each condition. The morphology and elemental distributions of the samples were investigated by SEM (Supra-55, Zeiss, Germany) and TEM (Themis Z, FEI, USA) equipped with EDS. The phase compositions of the samples were tested by XRD (X′pert PRO, PANalytical, Almelo, Netherlands), and the results were refined using GSAS software. To demonstrate the grain boundaries, the samples were treated with acid with $HF:HNO_3:H_2O$ = 1:1:3 at room temperature. The reconstructed 3D microstructure of the samples was acquired from an X-ray microscope (Xradia 610 Versa, CarlZeiss, Germany). The compression test of the samples (1.5 mm (in height) × 1 mm (in width) × 1 mm (in length)) was conducted using SUNS UTM2103 equipped with a 10 kN load cell. The compression rate of the test was 1 mm min^{-1}. High-temperature compression was carried out using a YKM-2200 testing machine under an Ar atmosphere. The heating rate was set to be 10 °C. The compression rate during the test was 0.05 mm min^{-1}. The thermal diffusivity α of samples (10 × 10 × 2 mm^3) was tested by a laser thermal conductivity instrument. The specific heat capacity C_p was measured by a differential scanning calorimeter (DSC, STA449F3, NETZSCH, Germany). The thermal conductivity σ_T of samples was calculated from $\sigma_T = \rho \times \alpha \times C_p$, where ρ is the density of samples measured by Archimedes drainage method. The thermal stability of the samples was tested using a high-temperature furnace under an Ar atmosphere. The furnace chamber was first vacuumed to below 10 Pa, and then filled with Ar gas to reach atmospheric pressure. This process was repeated three times. Subsequently, the furnace was heated at a rate of 5 °C min^{-1} to the desired temperatures (1000, 1500, and 2000 °C) for 60 min under an Ar atmosphere, followed by natural cooling to room temperature. The Weibull distribution of samples was calculated based on the following equation[71]

$$P_f = 1 - \exp\left(-\beta\sigma^m\right) \tag{6}$$

where m is the Weibull modulus, β is a factor related to the material, σ is the compressive strength of each sample, P_f is the probability of failure. Thus, $lnln(\frac{1}{1-P_f})$ was obtained by the linear regression fitting as follows

$$lnln\left(\frac{1}{1-P_f}\right) = mln\sigma + ln\beta \tag{7}$$

Supporting Information

Supporting Information is available from the Wiley Online Library or from the author.

Acknowledgements

The authors acknowledged the financial support from the National Key Research and Development Program of China (No. 2022YFB3708600), the National Natural Science Foundation of China (Nos. 52122204 and 51972116), and Guangzhou Basic and Applied Basic Research Foundation (No. 202201010632).

Conflict of Interest

The authors declare no conflict of interest.

Author Contributions

Z.W. and Z.T. contributed equally to this work. Y.C. conceived and designed this work. Z.W., L.Z., and Z.T. performed the experiments. Y.L. and H.Y. performed the first-principles calculations. Y.C., Z.W., L.Z., and Z.T. analyzed the data and wrote the manuscript. All authors commented on the manuscript.

Data Availability Statement

Data sharing is not applicable to this article as no new data were created or analyzed in this study.

Keywords

compressive strength, high-entropy diborides, high-temperature behaviors, porous materials, thermal conductivity

Received: November 8, 2023
Revised: December 27, 2023
Published online: January 6, 2024

[1] J. J. Bowen, S. Mooraj, J. A. Goodman, S. Peng, D. P. Street, B. Roman-Manso, E. C. Davidson, K. L. Martin, L. M. Rueschhoff, S. N. Schiffres, W. Chen, J. A. Lewis, M. B. Dickerson, *Mater. Today* **2022**, *58*, 71.
[2] F. Bouville, E. Maire, S. Meille, B. Van De Moortèle, A. J. Stevenson, S. Deville, *Nat. Mater.* **2014**, *13*, 508.
[3] J. T. Muth, P. G. Dixon, L. Woish, L. J. Gibson, J. A. Lewis, *Proc. Natl. Acad. Sci. USA* **2017**, *114*, 1832.
[4] L. Su, H. Wang, M. Niu, S. Dai, Z. Cai, B. Yang, H. Huyan, X. Pan, *Sci. Adv.* **2020**, *6*, eaay6689.
[5] D. Jang, L. R. Meza, F. Greer, J. R. Greer, *Nat. Mater.* **2013**, *12*, 893.
[6] J. Guo, S. Fu, Y. Deng, X. Xu, S. Laima, D. Liu, P. Zhang, J. Zhou, H. Zhao, H. Yu, S. Dang, J. Zhang, Y. Zhao, H. Li, X. Duan, *Nature* **2022**, *606*, 909.
[7] R. Yang, F. Hu, L. An, J. Armstrong, Y. Hu, C. Li, Y. Huang, S. Ren, *Nano Lett.* **2019**, *20*, 1110.
[8] J. Dittmann, J. Maurath, B. Bitsch, N. Willenbacher, *Adv. Mater.* **2016**, *28*, 1689.
[9] L. Han, F. Li, X. Deng, J. Wang, H. Zhang, S. Zhang, *J. Eur. Ceram. Soc.* **2017**, *37*, 2717.
[10] L. J. Gibson, M. F. Ashby, *Cellular Solids: Structure and Properties*, Cambridge University Press, Cambridge **1999**.
[11] T. Ohji, M. Fukushima, *Int. Mater. Rev.* **2012**, *57*, 115.
[12] C. Minas, D. Carnelli, E. Tervoort, A. R. Studart, *Adv. Mater.* **2016**, *28*, 9993.
[13] L. R. Meza, S. Das, J. R. Greer, *Science* **2014**, *345*, 1322.
[14] H. Gao, B. Ji, I. L. Jäger, E. Arzt, P. Fratzl, *Proc. Natl Acad. Sci. USA* **2003**, *100*, 5597.
[15] D. Lu, L. Zhuang, J. Zhang, L. Su, M. Niu, Y. Yang, L. Xu, P. Guo, Z. Cai, M. Li, K. Peng, H. Wang, *ACS Nano* **2023**, *17*, 1166.
[16] D. Mu, Z.-S. Liu, C. Huang, N. Djilali, *Microfluid. Nanofluid.* **2008**, *4*, 257.
[17] H. Liu, X. Zhao, *Int. J. Heat Mass Transfer* **2022**, *183*, 122089.
[18] Y. Li, Z. Zhang, R. Vogt, J. M. Schoenung, E. J. Lavernia, *Acta Mater.* **2011**, *59*, 7206.
[19] M. Ma, Y. Han, Z. Zhao, J. Feng, Y. Chu, *J. Materiomics.* **2023**, *9*, 370.
[20] A. Roy, P. Sreeramagiri, T. Babuska, B. Krick, P. K. Ray, G. Balasubramanian, *Mater. Charact.* **2021**, *172*, 110877.
[21] C. M. Rost, E. Sachet, T. Borman, A. Moballegh, E. C. Dickey, D. Hou, J. L. Jones, S. Curtarolo, J.-P. Maria, *Nat. Commun.* **2015**, *6*, 8485.
[22] X.-F. Wang, X.-G. Wang, Q.-Q. Yang, H.-L. Dong, C. Zhang, G.-J. Zhang, D.-Y. Jiang, *J. Am. Ceram. Soc.* **2021**, *104*, 2436.
[23] B. Ye, T. Wen, M. C. Nguyen, L. Hao, C.-Z. Wang, Y. Chu, *Acta Mater.* **2019**, *170*, 15.
[24] M. Yuan, X. Gao, X. Gu, C. Dong, S. Wang, M. Wen, K. Zhang, *J. Am. Ceram. Soc.* **2023**, *106*, 1356.
[25] J. Gild, Y. Zhang, T. Harrington, S. Jiang, T. Hu, M. C. Quinn, W. M. Mellor, N. Zhou, K. Vecchio, J. Luo, *Sci. Rep.* **2016**, *6*, 37946.
[26] J. L. Braun, C. M. Rost, M. Lim, A. Giri, D. H. Olson, G. N. Kotsonis, G. Stan, D. W. Brenner, J.-P. Maria, P. E. Hopkins, *Adv. Mater.* **2018**, *30*, 1805004.
[27] A. Giri, A. Z. Chen, A. Mattoni, K. Aryana, D. Zhang, X. Hu, S.-H. Lee, J. J. Choi, P. E. Hopkins, *Nano Lett.* **2020**, *20*, 3331.
[28] C. Wang, W. Ping, Q. Bai, H. Cui, R. Hensleigh, R. Wang, A. H. Brozena, Z. Xu, J. Dai, Y. Pei, C. Zheng, G. Pastel, J. Gao, X. Wang, H. Wang, J.-C. Zhao, B. Yang, X. R. Zheng, J. Luo, Y. Mo, B. Dunn, L. Hu, *Science* **2020**, *368*, 521.
[29] M. F. Ashby, *Philos. Trans. R. Soc., A* **2006**, *364*, 15.
[30] D. C. Jana, G. Sundararajan, K. Chattopadhyay, *J. Am. Ceram. Soc.* **2017**, *100*, 312.
[31] H. Wu, Y. Li, Y. Yan, J. Yin, X. Liu, Z. Huang, S.-H. Lee, D. Jiang, *J. Eur. Ceram. Soc.* **2014**, *34*, 3469.
[32] C. Ferraro, E. Garcia-Tuñon, V. G. Rocha, S. Barg, M. D. Fariñas, T. E. G. Alvarez-Arenas, G. Sernicola, F. Giuliani, E. Saiz, *Adv. Funct. Mater.* **2016**, *26*, 1636.

[33] Y.-H. Kim, Y.-W. Kim, W.-S. Seo, *J. Eur. Ceram. Soc.* **2020**, *40*, 2623.
[34] W. Huo, X. Zhang, Y. Chen, Y. Lu, J. Liu, S. Yan, J.-M. Wu, J. Yang, *J. Eur. Ceram. Soc.* **2018**, *38*, 2035.
[35] F. Yang, S. Zhao, W. Sun, K. Li, J. Chen, Z. Fei, Z. Yang, *J. Eur. Ceram. Soc.* **2023**, *43*, 521.
[36] F. Yang, S. Zhao, G. Chen, K. Li, Z. Fei, P. Mummery, Z. Yang, *Adv. Powder Mater.* **2023**, *3*, 100153.
[37] X. Li, M. Tao, M. Pan, W. Liu, Z. Gao, H. Yuan, C. Ma, *J. Eur. Ceram. Soc.* **2022**, *42*, 6015.
[38] L. Lin, H. Wang, C. Xia, J. Xu, X. Meng, R. Yang, G. Hu, Y. Qu, F. Gao, *J. Am. Ceram. Soc.* **2023**, *106*, 3800.
[39] Siddharth, P. Jana, S. Dietrich, S. Roy, *Mater. Sci. Eng. A.* **2023**, *864*, 144614.
[40] S. Chen, L. Wang, G. He, J. Li, C.-A. Wang, *J. Adv. Ceram.* **2022**, *11*, 172.
[41] L. Wang, L. An, J. Zhao, S. Shimai, X. Mao, J. Zhang, J. Liu, S. Wang, *J. Adv. Ceram.* **2021**, *10*, 852.
[42] S. M. Sajadi, L. Vásárhelyi, R. Mousavi, A. H. Rahmati, Z. Kónya, Á. Kukovecz, T. Arif, T. Filleter, R. Vajtai, P. Boul, Z. Pang, T. Li, C. S. Tiwary, M. M. Rahman, P. M. Ajayan, *Sci. Adv.* **2021**, *7*, eabc5028.
[43] C.-Q. Hong, J.-C. Han, X.-H. Zhang, J.-C. Du, *Scr. Mater.* **2013**, *68*, 599.
[44] Y. Qi, K. Jiang, C. Zhou, W. Han, Z. Du, *J. Eur. Ceram. Soc.* **2021**, *41*, 2239.
[45] X. Zhang, J. He, L. Han, Z. Huang, K. Xu, W. Cai, S. Wu, Q. Jia, H. Zhang, S. Zhang, *J. Eur. Ceram. Soc.* **2023**, *43*, 37.
[46] Z. Wu, L. Sun, P. Wan, J. Li, Z. Hu, J. Wang, *Scr. Mater.* **2015**, *103*, 6.
[47] Z. Wu, L. Sun, J. Pan, J. Wang, *Scr. Mater.* **2018**, *146*, 331.
[48] F. Li, Z. Kang, X. Huang, X.-G. Wang, G.-J. Zhang, *J. Eur. Ceram. Soc.* **2014**, *34*, 3513.
[49] S. Wang, M. Liu, X. Liu, Q. Jia, S. Zhang, *J. Eur. Ceram. Soc.* **2022**, *42*, 4465.
[50] H. Chen, H. Xiang, F.-Z. Dai, J. Liu, Y. Zhou, *J. Mater. Sci. Technol.* **2019**, *35*, 2778.
[51] Z. Wei, Z. Zhang, X. Zhang, Z. Li, T. Li, J. Hu, S. Xu, Z. Shi, *J. Mater. Sci. Technol.* **2022**, *100*, 161.
[52] Y.-W. Kim, Y.-J. Jin, Y.-S. Chun, I.-H. Song, H.-D. Kim, *Scr. Mater.* **2005**, *53*, 921.
[53] M. Sutcu, S. Akkurt, *J. Eur. Ceram. Soc.* **2010**, *30*, 1785.
[54] L. Wu, C. Li, H. Li, H. Wang, W. Yu, K. Chen, X. Zhang, *Int. J. Appl. Ceram. Technol.* **2020**, *17*, 963.
[55] M. L. Sandoval, M. A. Camerucci, A. G. Tomba Martinez, *J. Mater. Sci.* **2012**, *47*, 8013.
[56] X. Wu, Y. Ranglack-Klemm, J. Hubálková, J. Solarek, C. G. Aneziris, A. Weidner, H. Biermann, *Ceram. Int.* **2021**, *47*, 3920.
[57] X. Wu, A. Weidner, C. G. Aneziris, H. Biermann, *Ceram. Int.* **2023**, *47*, 13140.
[58] A. Muñoz, J. Marti Nez Fernández, M. Singh, *J. Eur. Ceram. Soc.* **2002**, *22*, 2727.
[59] B. Han, R. Zhang, D. Fang, *J. Porous Mater.* **2016**, *23*, 563.
[60] Y. Liu, H. Tang, M. Ma, H. Yu, Z. Tang, Y. Chu, **2023**, arXiv:2312.09574 [cond-mat.mtrl-sci].
[61] F. Wakai, Y. Kodama, S. Sakaguchi, N. Murayama, K. Izaki, K. Niihara, *Nature* **1990**, *344*, 421.
[62] H. Chen, H. Xiang, F.-Z. Dai, J. Liu, Y. Zhou, *J. Mater. Sci. Technol.* **2019**, *35*, 2404.
[63] S. Wang, Y. Yang, J. Cui, X. Liu, S. Zhang, Q. Jia, *Ceram. Int.* **2022**, *48*, 27051.
[64] N. Yan, Q. Fu, Y. Zhang, K. Li, W. Xie, J. Zhang, L. Zhuang, X. Shi, *Ceram. Int.* **2020**, *46*, 19609.
[65] Q. Yang, C. Li, H. Ouyang, R. Gao, T. Shen, J. Huang, *Materials* **2023**, *16*, 2495.
[66] H. Chen, H. Xiang, F.-Z. Dai, J. Liu, Y. Lei, J. Zhang, Y. Zhou, *J. Mater. Sci. Technol.* **2019**, *35*, 1700.
[67] L. Han, Y. Chen, H. Zhang, G. Li, Q. Jia, S. Zhang, *J. Am. Ceram. Soc.* **2023**, *106*, 841.
[68] Z. Wu, X. Liang, Z. Shao, H. Chen, J. Li, J. Wang, *J. Am. Ceram. Soc.* **2021**, *18*, 101158.
[69] F. Hu, S. Wu, Y. Sun, *Adv. Mater.* **2019**, *31*, 1801001.
[70] K. Zhao, F. Ye, L. Cheng, J. Yang, X. Chen, *J. Eur. Ceram. Soc.* **2023**, *43*, 7241.
[71] R. Danzer, P. Supancic, J. Pascual, T. Lube, *Eng. Fract. Mech.* **2007**, *74*, 2919.